

PAPER

Evidence of oxygen vacancy induced room temperature ferromagnetism in solvothermally synthesized undoped TiO₂ nanoribbons

Cite this: *Nanoscale*, 2013, 5, 5476

Batakrushna Santara,^a P. K. Giri,^{*ab} Kenji Imakita^b and Minoru Fujii^b

We report on the oxygen vacancy induced ferromagnetism (FM) at and above room temperature in undoped TiO₂ nanoporous nanoribbons synthesized by a solvothermal route. The origin of FM in as-synthesized and vacuum annealed undoped nanoribbons grown for different reaction durations followed by calcinations was investigated by several experimental tools. X-Ray diffraction pattern and micro-Raman studies reveal the TiO₂(B), TiO₂(B)-anatase, and anatase–rutile mixed phases of TiO₂ structure. Field emission scanning electron microscopy and transmission electron microscopy observations reveal nanoribbons with uniform pore distribution and nanopits/nanobricks formed on the surface. These samples exhibit strong visible photoluminescence associated with oxygen vacancies and a clear ferromagnetic hysteresis loop, both of which dramatically enhanced after vacuum annealing. Direct evidence of oxygen vacancies and related Ti³⁺ in the as-prepared and vacuum annealed TiO₂ samples are provided through X-ray photoelectron spectroscopy analysis. Micro-Raman, infrared absorption and optical absorption spectroscopic analyses further support our conclusion. The observed room temperature FM in undoped TiO₂ nanoribbons is quantitatively analyzed and explained through a model involving bound magnetic polarons (BMP), which include an electron locally trapped by an oxygen vacancy with the trapped electron occupying an orbital overlapping with the unpaired electron (3d¹) of Ti³⁺ ion. Our analysis interestingly shows that the calculated BMP concentration scales linearly with concentration of oxygen vacancies and provides a stronger footing for exploiting defect engineered ferromagnetism in undoped TiO₂ nanostructures. The development of such highly porous TiO₂ nanoribbons constitutes an important step towards realizing improved visible light photocatalytic and photovoltaic applications of this novel material.

Received 14th February 2013

Accepted 31st March 2013

DOI: 10.1039/c3nr00799e

www.rsc.org/nanoscale

Introduction

Dilute magnetic semiconductors (DMS), in particular the ferromagnetic oxides, have been at the forefront of research for spintronics and magneto-optic device materials.^{1–3} The discovery of ferromagnetism in Co-doped TiO₂ with a Curie temperature (T_C) exceeding 300 K (ref. 3) was crucial in expanding the field of DMS to oxides, leading to a rapid development of new materials and phenomena arising from a synergy of semiconductor physics and strongly correlated systems. As a result, intensive attention has been focused on DMS such as transition metals (TM) doped ZnO,⁴ SnO₂,⁵ In₂O₃,⁶ and TiO₂ (ref. 7) due to realization of room temperature ferromagnetism (RTFM) in these systems. Among various oxide based DMS, TiO₂ has drawn extensive research interest because it is an excellent photo-catalyst for water splitting and it

possesses good optical transmission in the visible and near infrared region making it a suitable candidate for magneto-optic devices as well. However, in spite of several studies reported on TiO₂-based DMS, there is no clear agreement about the nature and origin of the observed ferromagnetism (FM). It is being currently debated whether the observed FM in oxide DMS has anything to do with TM doping or might be solely related to intrinsic defects. Some reports suggested segregation and the formation of Co clusters as the origin of FM signal,^{8,9} while most recent results strongly support the intrinsic nature of FM mediated by carriers or defects.^{7,10,11} These controversial results among research groups suggest that the magnetic properties of DMS materials are critically dependent on fabrication, growth conditions, and doping agents. Compared to other methods of preparation, solvothermal method is very simple, low cost, and one can easily tune the surface defects by controlling the growth temperature, reaction duration *etc.*

Interestingly, some of the outstanding works revealed no evidence of ferromagnetic ordering of the active doped metal in Co, Mn doped ZnO systems.^{12–14} Using *ab initio* electronic structure calculation, Pandey and Choudhary¹⁵ argued that an

^aDepartment of Physics, Indian Institute of Technology Guwahati, Guwahati 781039, India. E-mail: giri@iitg.ernet.in

^bDepartment of Electrical and Electronic Engineering, Graduate School of Engineering, Kobe University, Kobe 657-8501, Japan

oxygen vacancy leads to electron doping in TiO_2 system, but does not induce an appreciable magnetic moment. More recently, Hoa and Huyen¹⁶ reported enhanced FM in undoped TiO_2 nanowire as compared to Ni doped TiO_2 nanowire. Further, RTFM have been observed in a wide range of undoped oxides such as TiO_2 ,¹⁷ HfO_2 ,¹⁸ In_2O_3 ,¹⁷ SnO_2 ,¹⁹ ZnO ,²⁰ and Al_2O_3 .²¹ These help to settle the controversies about the issues related to the role of defects in the ferromagnetic ordering. In fact, Sundaresan and Rao suggested FM as a universal feature of inorganic nanoparticles where the FM was confined to the surface of the nanoparticles.²² However, unambiguous determination of the nature of defects responsible for the observed FM remains a considerable challenge to the researchers. It is unclear whether oxygen vacancy or Ti vacancy defects contribute to the magnetic moments, since both titanium and oxygen vacancies were proposed to be responsible for the FM in undoped TiO_2 . On the other hand, theoretical²³ studies indicated that cation vacancies and divacancies are ferromagnetically coupled. Interestingly, more and more theoretical and experimental^{24,25} evidences show that the magnetic ordering of undoped TiO_2 is strongly related to oxygen vacancy and thus it was thought to be source of RTFM in undoped semiconducting oxides.

Till date, most of the reported FM in undoped TiO_2 was for thin films^{11,17,24,25} and nanoparticles.^{22,26} The observed FM in undoped thin films and nanoparticles are usually weak and might originate from surface defects such as oxygen vacancies and/or interface defects. Compared to thin films and nanoparticles, 1D TiO_2 nanostructures such as nanowires, nanorods and nanoribbons with high surface area can possess abundant surface defects, thus the intrinsic FM could be enhanced. Moreover, 1D nanostructures are favoured compared to nanoparticles in terms of electron transport, storage and information processing that can enhance the performance of spintronic devices at the nanoscale for practical applications. Although little information about the magnetic properties of 1D anatase TiO_2 nanowire,²⁷ rutile TiO_2 nanowire,¹⁶ and vanadium doped $\text{TiO}_2(\text{B})$ ²⁸ nanotubes are available in the literature, to the best of our knowledge, there is no report on the intrinsic RTFM in undoped $\text{TiO}_2(\text{B})$ nanoporous nanoribbons. Our present attempt in this study is to enhance the magnetic moments which are solely due to intrinsic defects and explore a better understanding about the origin of observed ferromagnetism in undoped 1D TiO_2 system.

Here, we grow TiO_2 nanoporous nanoribbons by an ethylene glycol mediated solvothermal method and studied the effect of reaction duration and calcination temperature on the surface morphology; we investigate the optical and magnetic properties and the origin of RTFM in the undoped TiO_2 nanoribbons. The high surface area and higher concentration of surface defects, such as oxygen vacancies, expected in these nanoporous nanoribbons could ultimately lead to enhanced ferromagnetic ordering and strong ferromagnetism even at room temperature. It will be demonstrated that a large concentration of oxygen vacancies with high thermal stability indeed results in stronger RTFM compared to those previously reported in undoped/doped TiO_2 systems.

Experimental

Growth and processing of TiO_2 nanoribbons

Anatase TiO_2 powders (average particle size ~ 80 nm), sodium hydroxide pellets (NaOH), and ethylene glycol were used as received from Merck. Doubly distilled deionized (DI) water was used during all the experiments. In a typical synthesis, 0.275 g of anatase TiO_2 powder was mixed with 60 ml of 10 M NaOH in mixed solvent (DI water : Ethylene glycol = 1 : 1) under stirring for 1 h, a milky solution was obtained. Afterwards, the mixed solution was transferred into a Teflon-lined autoclave (Berghof, BR-100) of 100 ml capacity. The temperature inside the autoclave was monitored and maintained at 180 °C under autogenous pressure and constant magnetic stirring at 250 rpm for 16–48 h. The formed precipitates were obtained by centrifugation and washed several times with DI water. Then the products underwent an ultrasonic treatment with 0.1 M HCl till the pH ~ 7 and finally the precipitates were calcined at different temperatures in the range 500–900 °C for 5 h in air. The vacuum annealing of the sample grown for 16 h followed by 500 °C calcination was performed at 300 °C under 1.2×10^{-2} mbar pressure for 2 h. For convenience of discussion, the TiO_2 nanoribbon samples are named as S1, S2, S3 for samples grown after a reaction duration of 16 h and calcinations at 500 °C, 700 °C, and 900 °C, respectively. The sample S1 after vacuum annealing is named as S4. Samples grown after a reaction time of 24 h followed by calcinations at 500 °C and 900 °C are termed as S5 and S6, respectively. Samples grown after a 48 h reaction followed by calcination at 500 °C are termed as S7, as presented in Table 1.

Characterization

The crystal structures of the obtained samples are characterized by X-ray diffraction (XRD) (Rigaku RINT 2500 TTRAX-III, Cu $K\alpha$ radiation) and micro-Raman spectroscopy (LabRam HR800, Jobin Yvon). Morphologies of the samples were studied by a field emission scanning electron microscopy (FESEM) (Sigma, Zeiss). The energy dispersive X-ray spectrum was studied by scanning electron microscopy (SEM, LEO 1430VP). The high magnification surface morphologies and structures of the samples were studied by transmission electron microscopy (TEM), high-resolution TEM (HRTEM) and selected area electron diffraction (SAED) pattern (JEOL-JEM 2010 operated at 200 kV). Specimens for HRTEM investigations were prepared by dispersing powder particles in ethanol and drop casting it on a carbon coated copper grid of 400 meshes (Pacific Grid, USA). The UV-vis absorption spectroscopy measurements were recorded using a commercial spectrophotometer (PerkinEmler UV win Lab). The steady state photoluminescence (PL) spectrum was recorded at room temperature by using a 325 nm He–Cd laser excitation with the help of a spectrometer (focal length: 15 cm; blaze wavelength: 500 nm; groove density: 150 g mm^{-1}) equipped with a cooled charge-coupled device (Princeton Instruments, PIXIS 100B) detector. The power samples were put on a conductive carbon tape (black) for the PL measurements. Each spectrum was corrected for the detector response as a

Table 1 Details of the samples studied with change in Raman modes, integrated PL intensity due to oxygen vacancy (O_v) and relative area (%) under the Ti^{3+} and O_v peaks in the XPS spectra

Sample name	Growth duration, calcination	Crystal structure	Nanoribbon surface features	$E_g(1)$ frequency and FWHM (cm^{-1})	Integrated PL intensity (a.u.)	Ti^{3+} % in Ti 2p _{3/2} XPS spectrum	O_v % in O 1s XPS spectrum
S1	16 h, 500 °C	TiO ₂ (B)	Nanopits	146.7 (18.3)	25.6	9%	70%
S2	16 h, 700 °C	TiO ₂ (B)-anatase	Nanobricks	143.5 (10.3)	121.5	—	—
S3	16 h, 900 °C	Anatase-rutile	Smooth	145.1 (11.5)	206.3	—	—
S4	S1 Vac. anneal	TiO ₂ (B)	—	146.8 (23.3)	2555.2	15%	83%
S5	24 h, 500 °C	TiO ₂ (B)	Nanobricks	142.8 (5.5) 147.8 (11.1)	1587.8	—	—
S6	24 h, 900 °C	Anatase-rutile	—	143.8 (11.1)	—	—	—
S7	48 h, 500 °C	TiO ₂ (B)	Nanobricks	143.9 (12.7)	736.9	—	—
Precursor-TiO ₂	—	Anatase	—	142.0 (7.6)	2840.2	—	—

function of wavelength after background subtraction. The Fourier transform infrared (FTIR) spectra were measured in the range 400–4000 cm^{-1} with FTIR spectrometer (Perkin Elmer, Spectrum BX) using KBr wafer. The magnetic properties of the samples were measured by using a Lakeshore (Model no. 7410) vibrating sample magnetometer (VSM). X-Ray photoelectron spectroscopy (XPS) measurements were carried out with an ESCALAB 3400 photoelectron spectrometer (Shimadzu, Japan) using Mg K α X-ray beam (1253.6 eV) with a beam current of 20 mA. Carbon 1s spectrum was used for the calibration of the XPS spectra recorded for various samples.

Results and discussion

Structural characterization

The XRD patterns of solvothermal products synthesized after different reaction durations and calcinations are shown in Fig. 1. All the peaks correspond to TiO₂(B) phase for the sample S1; however, for the samples S2 and S3, mixed phase TiO₂(B)–anatase and anatase–rutile TiO₂ with little signature of TiO₂(B) are observed, respectively which are shown in Fig. 1(a). From the Fig. 1(b), we observed that pure TiO₂(B) phase formed at 180 °C after 500 °C calcinations irrespective of reaction duration (samples S1, S5, S7). Fig. 1(c) shows the XRD patterns of the samples before HCl treatment and after HCl treatment prior to the calcination. This indicates that the sample prior to HCl treatment corresponds to Na₂Ti₄O₉ (PCPDF # 33-1294) structure and after HCl treatment, Na⁺ ion is replaced by H⁺ ion and formed H₂Ti₅O₁₁·H₂O (PCPDF # 44-0131). The calcination process helps in dehydration of H₂Ti₅O₁₁·H₂O to form TiO₂ structures. This indicates that calcination temperatures play an important role for the formation of different phases of TiO₂. Each phases has important application for different technological application point of view such as pure TiO₂(B) is favourite for Li-ion storage,²⁹ mixed phase TiO₂(B)–anatase and mixed phase anatase–rutile have potential application for enhancing photocatalytic effect.³⁰ It is reported that TiO₂(B)

phase is a metastable form of TiO₂ and generally obtained in high pressure hydrothermal method and converted to anatase phase upon heating at higher temperature and it is difficult to synthesize pure TiO₂(B) phase. However, we are able to

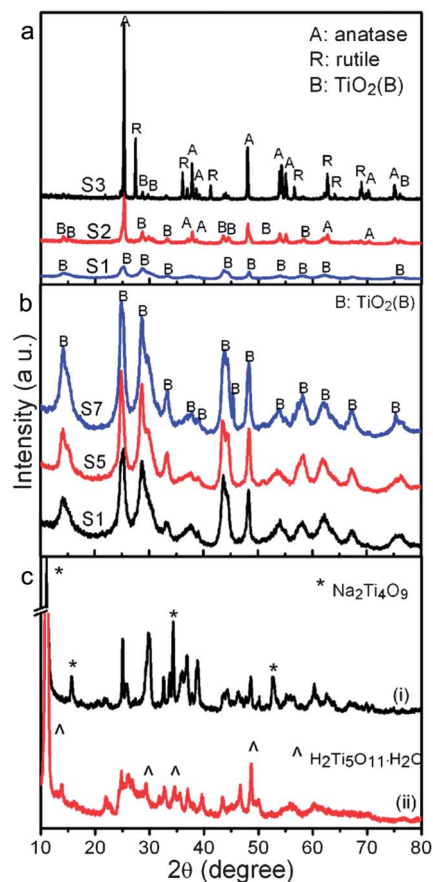


Fig. 1 XRD patterns: (a) samples S1, S2, S3 (b) samples S1, S5, S7 (c) sample grown after 16 h; (i) before HCl treatment and (ii) after HCl treatment, prior to calcination.

synthesize pure $\text{TiO}_2(\text{B})$ phase nanoporous nanoribbons and observed room temperature ferromagnetism in this study, which is a significant development for future applications.

Raman scattering studies

Raman scattering is one of the most powerful tools for the study of crystallinity, phase composition, phonon confinement effect and defect structures associated with the material. More importantly, the XRD patterns for sodium titanates, hydrogen titanates and different polymorphs of TiO_2 (anatase, rutile, brookite) are quite similar. Therefore, XRD patterns may not give a conclusive idea about the structure and phase composition of TiO_2 nanoribbons. Hence, the as-synthesized and vacuum annealed samples are further characterized by Raman spectroscopy to clarify the structure, phase composition, strain and defects present in the materials. All the Raman peaks of the sample S1 correspond to the $\text{TiO}_2(\text{B})$ phase as shown in Fig. 2(a). From Fig. 2(a), it can be noted that the Na-titanate and H-titanate phases are formed before HCl treatment and after HCl treatment prior to calcinations. This again confirms that when TiO_2 precursor powder reacts with NaOH, it forms Na-titanate and after HCl treatment it is converted to H-titanate and finally converted to various phases of TiO_2 during calcinations at different temperatures. The Raman modes for the samples S2, S3, and S6 show the mixed phase $\text{TiO}_2(\text{B})$ -anatase and anatase-rutile, respectively shown in Fig. 2(b) and this is consistent with the XRD analysis. The six active Raman modes $E_g(1)$, $E_g(2)$, $B_{1g}(1)$, A_{1g} , $B_{1g}(2)$ and $E_g(3)$ are assigned to anatase TiO_2 . The Raman modes at 121 cm^{-1} and 427 cm^{-1} (low intensity) for the sample S2 are assigned to B_g and A_g modes of $\text{TiO}_2(\text{B})$, respectively,³¹ whereas the Raman modes at 441 cm^{-1} and 612 cm^{-1}

for the sample S6 are assigned to E_g and A_{1g} modes of rutile TiO_2 , respectively. The most intense $E_g(1)$ Raman mode of anatase at 142.0 cm^{-1} in precursor TiO_2 is found to be blue shifted for all the as-synthesized samples by about $2\text{--}6\text{ cm}^{-1}$, as detailed in Table 1. In particular, the blue shift and full width at half maximum (FWHM) is highest for the sample S4. Comparison of the Raman shift and FWHM for sample S3 and S4 are shown in Fig. 2(c) and (d), respectively. As compared to S3, FWHM of the $E_g(1)$ mode is more than doubled in S4. Similar changes are observed for the B_{1g} mode at 397 cm^{-1} (not shown). Such a blue shift and higher FWHM of the $E_g(1)$ Raman mode was interpreted as a different competing mechanism such as non-stoichiometry due to oxygen vacancies or disorder induced defects and phonon confinement effects.^{32,33} It has been reported that defects and disorder in TiO_2 nanostructures affect the B_{1g} mode more strongly than the $E_g(1)$ mode. In the present study, we notice systematic changes in both the modes revealing a strong presence of defects. From FESEM and TEM images, we observed that the size of the nanoribbons is too large to induce phonon confinement effect and it is often orders of magnitude larger than the size of the precursor TiO_2 nanoparticles. So, the phonon confinement effect is easily discarded. Therefore, we believe that the blue-shift and increase in FWHM in as-synthesized and vacuum annealed nanoribbons is due to the reduced oxygen stoichiometry in the as-grown nanostructures. Further, we notice a relative decrease in intensity of the A_g mode after vacuum annealing of S1, while that of B_g mode remains unchanged, as shown in the inset of Fig. 2(b). Similarly, the B_g mode of S1 at 194 cm^{-1} is red shifted to 192 cm^{-1} after vacuum annealing (sample S4) indicating the introduction of additional defects, *e.g.* oxygen vacancies, by annealing in reduced atmosphere. Thus, Raman studies revealed that nonstoichiometric defects are present in the as-grown nanoribbons and additional defects are created by annealing the sample in reduced atmosphere, as expected.

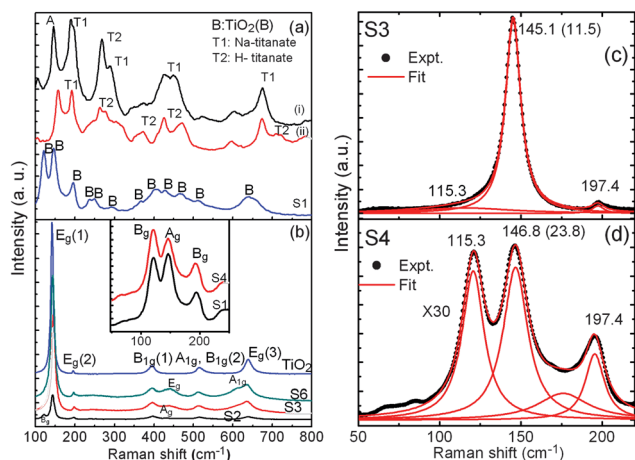


Fig. 2 Raman Spectra for the TiO_2 nanoribbons: (a) grown after 16 h reaction (i) before HCl treatment, (ii) after HCl treatment (prior to calcination), and (S1) after calcination at 500°C . (b) Comparison of intensity for S2, S3, S6 and precursor TiO_2 ; inset shows the relative changes in intensity for A_g mode at 146.6 cm^{-1} in S1 and S4. Peak positions are marked with standard notations (*e.g.*, see ref. 31). (c) Fitted spectra (solid line) with Lorentzian line shapes for S3 and (d) fitted spectra (solid line) with Lorentzian line shape for S4. Experimental data are shown with symbols. Peak positions are marked with corresponding wave number (cm^{-1}), bracketed number shows full width at half maximum in cm^{-1} .

Morphology studies

The morphologies of the as-synthesized nanostructures as observed by FESEM are shown in Fig. 3. The low magnification image of sample S1 (Fig. 3(a)) shows long and straight nanoribbons of TiO_2 . The corresponding high magnification image of the sample shows well resolved nanopits on the surface of the nanoribbons, as shown in Fig. 3(b). Fig. 3(c) shows the magnified image of sample S2, where nanoribbons with a nanobrick-like structure on the surface are observed. However, nanoribbons with smooth surfaces are observed for the sample S3, *i.e.*, after higher temperature (900°C) calcination, as shown in Fig. 3(d). Thus the calcination temperature plays a vital role for the formation of different surface morphologies on the nanoribbons. The EDX spectrum of nanoribbons is shown in the inset of Fig. 3(a), which shows only Ti, O elements indicating that the pure TiO_2 phase is formed after HCl treatment and calcinations. This is consistent with XRD and Raman analyses, as there is no signature of Na or H-titanate.

Fig. 4(a)–(c) show the TEM images of the sample S1. Fig. 4(b) shows the high magnification TEM image of a single

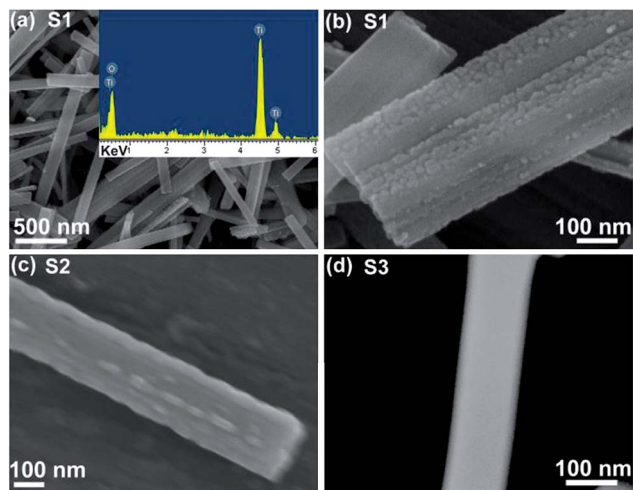


Fig. 3 FESEM images of the morphology of the 1D TiO_2 nanostructures: (a) S1 (low magnification), inset shows the EDX spectrum; and (b) S1 (high magnification); (c) S2 and (d) S3.

nanoribbon having well resolved nanopits of uniform shapes and sizes (diameter ~ 8 nm) on the surface of the nanoribbon. The SAED pattern of the corresponding nanoporous

nanoribbon is shown in the inset of Fig. 4(a), which indicates the single crystalline nature of $\text{TiO}_2(\text{B})$ phase. The (110) crystal plane of $\text{TiO}_2(\text{B})$ is indexed in the figure. A typical HRTEM image of the nanoribbon is shown in Fig. 4(c), the clear lattice fringe indicates that the as-synthesized products are well crystalline. The d -spacing of 3.43 \AA corresponds to the (110) crystal plane of $\text{TiO}_2(\text{B})$ phase, which is also the highest intensity peak observed in the XRD pattern. The TEM images of sample S2 are shown in Fig. 4(d)–(f). Here again, nanoribbons with nanobrick and nanopit-like structures on the surface are clearly observed in high magnification image in Fig. 4(e). The nanopits of diameter $5\text{--}13$ nm and nanobricks of width ~ 13 nm are formed on the surface of nanoribbons making them porous like structures, with highly active surface. The inset of Fig. 4(d) shows the corresponding SAED pattern. It clearly dictates the tetragonal pattern of anatase TiO_2 and monoclinic pattern of $\text{TiO}_2(\text{B})$ phase indicating mixed phase $\text{TiO}_2(\text{B})$ -anatase is formed. The electron diffraction spots of monoclinic nature are joined by lines shown in the inset of Fig. 4(d). Fig. 4(f) shows the HRTEM lattice fringe with a d -spacing of 5.82 \AA and 2.59 \AA corresponding to (200) and (310) plane of $\text{TiO}_2(\text{B})$ phase, respectively. This indicates that the nanoribbons are grown along the $\langle 200 \rangle$ direction whereas the nanobricks are grown along the $\langle 310 \rangle$

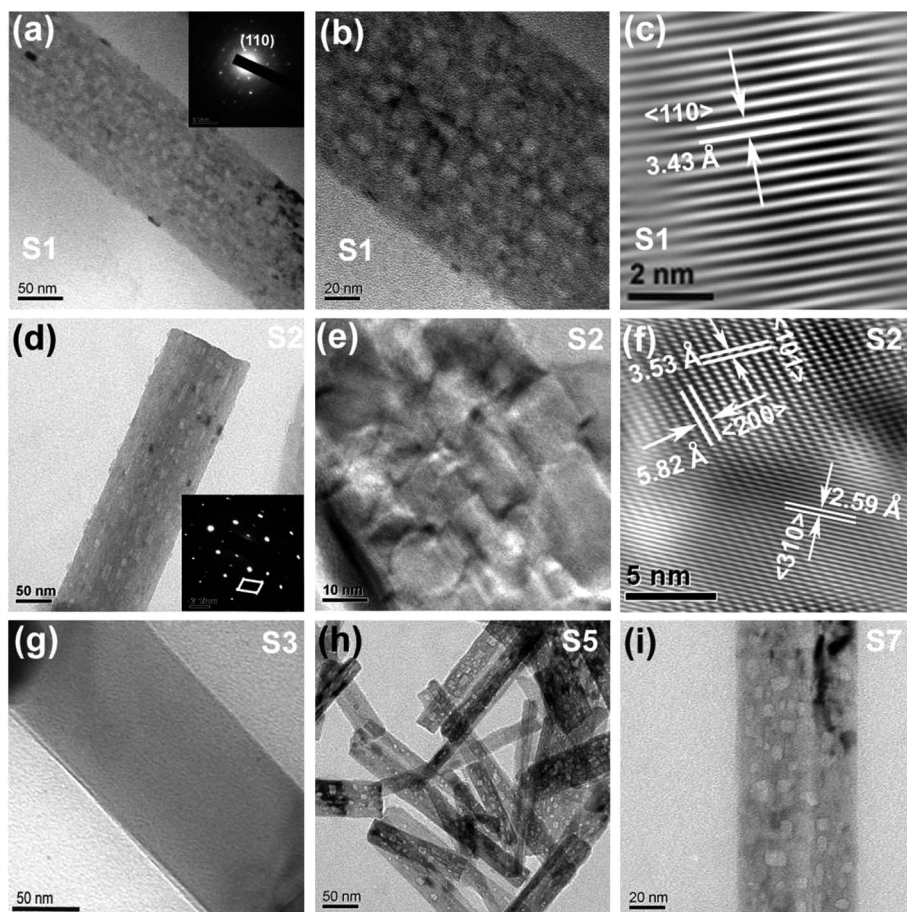


Fig. 4 TEM images: (a) S1, (b) S1 at higher magnification showing nanopits, (c) S1, lattice fringe, (d) S2, (e) S2 at higher magnification showing nanobricks, (f) S2, lattice fringe, (g) S3 showing smooth surface, (h) S5 with nanobricks, (i) S7 with nanobricks. The inset in (a) and (d) shows the corresponding SAED patterns.

direction. The d -spacing of 3.53 Å corresponds to (101) plane of anatase TiO_2 . Fig. 4(g) shows the TEM image of the sample S3. Nanoribbons with smooth surface are formed after 900 °C calcination. The TEM images are fully consistent with the FESEM images. Thus, from the TEM images, it is further concluded that nanoribbons with nanopits, nanobricks and nanoribbons with smooth surface are formed at 180 °C after calcinations at 500, 700 and 900 °C, respectively. The chelating properties of ethylene glycol may have helped for the formation of nanoporous structure. The parent TiO_6 octahedra of TiO_2 materials may coordinate with glycol to form chain-like structure,³⁴ whereas the NaOH may form titanate nanosheets by sharing the vertices edges of the octahedra and resulting nanoribbons with nanopits are formed at 180 °C after 16 h and 500 °C calcination. However, as the calcination temperature increases to 700 °C, the nanobricks are grown along the $\langle 310 \rangle$ direction and fewer nanopits are present. After 900 °C calcination, the bonds between Ti–O may rearrange to form a smooth surface. Fig. 4(h) and (i) show the TEM images of samples S5 and S7, respectively. In both the cases, nanoporous nanoribbons with nanobricks on the surface are observed with no nanopits. Thus, reaction duration plays the important role to tune the surface morphology and this is crucial in tuning the electronic, optical and magnetic properties of the nanostructures.

Optical absorption and photoluminescence studies

Light absorption characteristics of the solvothermally synthesized 1D TiO_2 nanostructures and the precursor TiO_2 are shown in Fig. 5. All the as-synthesized samples exhibit a red shift of the absorption edge and considerable absorption in the visible region (>420 nm). With the increase in calcination temperature from 500 to 700 °C, the absorption edge shows slight blue shift whereas it is again red shifted for the sample calcined at 900 °C. It is reported that the bandgap of $\text{TiO}_2(\text{B})$, anatase and rutile TiO_2 are 3.1, 3.2 and 3 eV,³⁰ respectively. Since there is a phase

transition from $\text{TiO}_2(\text{B})$ to mixed phase $\text{TiO}_2(\text{B})$ –anatase and mixed phase anatase–rutile with calcination temperatures from 500–900 °C, respectively, the blue shift and red shift of absorption edges are expected. Interestingly, a clear absorption band at ~484 nm for the samples S1 and S2 indicates the transition involving oxygen vacancy-related intermediate deep trap states, which is shown in the inset of Fig. 5. Theoretical calculations suggested that a high vacancy concentration could induce a vacancy band of electronic states just below the conduction band.³⁵ Zuo *et al.*³⁶ reported that the presence of a miniband closely below the conduction band minimum which is related to the oxygen vacancy associated with Ti^{3+} and is responsible for the bandgap narrowing in TiO_2 . A similar observation related to oxygen vacancy induced bandgap narrowing has been reported in a ZnO system.³⁷ Recently, Hoang *et al.*³⁸ reported that interaction between Ti^{3+} and N modified the band structure of TiO_2 and are responsible for the enhancement in the water oxidation performance under visible light illumination. Note that the absorption edge of precursor TiO_2 powder is at 380 nm, the large red shift of the as-synthesized nanoribbons may be due to the shallow trap states created by oxygen vacancies associated with Ti^{3+} , leading to a bandgap narrowing. This is important in achieving visible light photocatalysis and exploring other applications of TiO_2 without introducing any external doping/impurities for practical applications.

In order to confirm the nature of defects, PL studies are performed on different samples. Fig. 6(a) shows the room temperature PL spectra of samples S1–S7 under identical conditions of measurement. Due to an indirect bandgap, no band edge emission was detected, therefore excluding the free exciton recombination. The observed broad visible luminescence is primarily related to self trapped excitons and oxygen vacancy related defect states in $\text{TiO}_2(\text{B})$ phase. Note that the PL

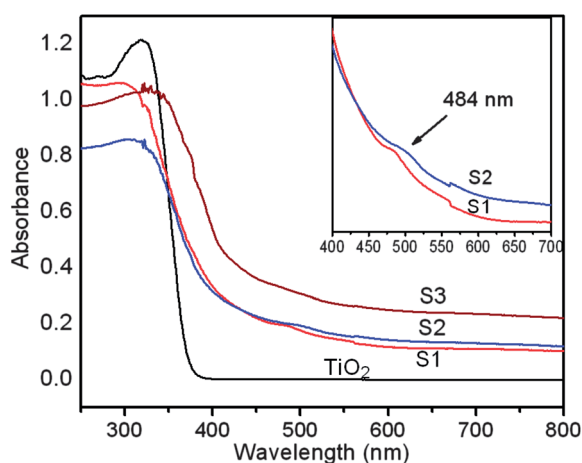


Fig. 5 UV-vis absorption spectra: precursor TiO_2 , S1, S2, S3. As-synthesized nanostructures show a clear red-shifted band compared to precursor TiO_2 . The inset shows the magnified view of the absorption band related to deep trap states (defects).

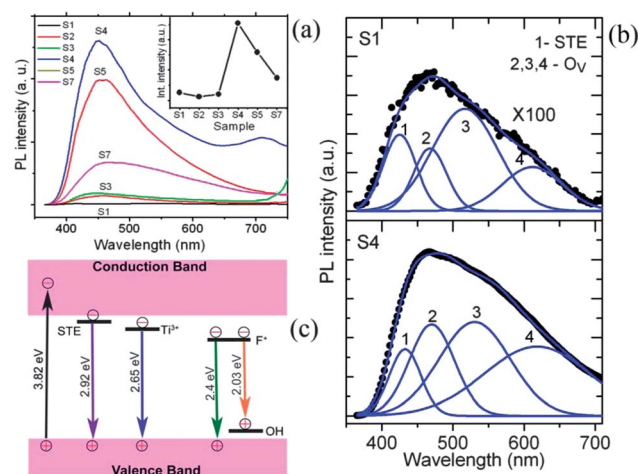
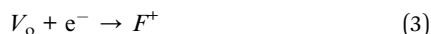
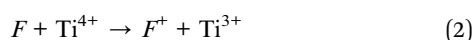


Fig. 6 Room temperature PL spectra in the visible region: (a) S1, S2, S3, S4, S5, and S7, inset shows the integrated PL intensity for different samples; (b) comparison of PL intensity for S1 and S4. Each spectrum was fitted with four Gaussian peaks (1, 2, 3 and 4). The deconvoluted spectra are shown with solid lines and experimental data are shown with symbols. (c) Schematic diagram illustrating the physical origin of visible PL emissions. See text for details.

intensity is lowest for the sample S1, while it is highest for S4, about 2 orders of magnitude higher in intensity than that of S1, as shown in Fig. 6(b). The inset of Fig. 6(a) shows the integrated PL intensity for various samples. For a clearer understanding of the origin of the broad PL emission, the deconvolution of the peak was necessary. The broad emission peak could be fitted properly with four Gaussian bands centred at 425.0 (peak 1), 467.7 (peak 2), 516.8 (peak 3), 611.7 (peak 4) nm for S1 and at 432.6 (peak 1), 470.1 (peak 2), 530.5 (peak 3), 618.3 (peak 4) for S4, respectively as shown by the solid lines (blue curves). According to the literature, peak 1 may be ascribed to self trapped excitons located at TiO_6 octahedra, while peak 2 and 3 are ascribed to oxygen vacancy related trap states.³⁹ Peak 4 is not reported earlier, though it is likely to be related to an intrinsic defect.

It is reported that the visible luminescence band originates from the oxygen vacancies associated with Ti^{3+} in anatase TiO_2 .³⁹ More importantly, the PL emission is enhanced by about two orders of magnitude in the vacuum annealed sample S4 as compared to S1, strongly indicating that concentration of oxygen vacancies are dramatically high in vacuum annealed samples, as expected. Similarly, the PL intensity is high for S5. From the XPS analyses, it will be evident that the TiO_2 nanoribbons are primarily oxygen deficient. Upon the loss of an O atom in TiO_2 lattice, the electron pair that remains trapped in the vacancy cavity V_o left behind a pair of electrons which give rise to an F center (eqn (1)).⁴⁰ The basic assumption is that one of the electron in F centre tends to occupy the neighboring Ti^{4+} ion and yield Ti^{3+} center and F^+ center (eqn (2)) forming a shallow and deep trap states, respectively which is explained in the following equations.



thus, Ti^{3+} center and F^+ center (single electron associated with oxygen vacancies) are formed due to the absence of an oxygen atom. Shallow trap states identified with oxygen vacancies were established at 0.51⁴¹ and 0.8 eV (ref. 42) below the conduction band. The PL peak at 467.7 nm is coincident with shallow trap which can be assigned to Ti^{3+} states just below the conduction band, while PL emission at 516.8 nm is due to deep trap state which is associated with the F^+ center.⁴³ The location of these trap centres responsible for the strong visible PL from TiO_2 nanoribbons can be understood from the schematic band diagram shown in Fig. 6(c). The photogenerated electrons are initially excited to the conduction band of TiO_2 on irradiating UV-light (325 nm) and then relaxed to the defect states. The defect states in TiO_2 are attributed to three different physical origins: self trapped exciton, oxygen vacancies and surface states. The emission at 425.0 nm originates from the self trapped excitons (STE) localized in TiO_6 octahedra.⁴³ The emission at 467.7 nm is attributed to shallow trap states originated from

oxygen vacancies associated with Ti^{3+} , while the emission at 516.8 nm is attributed to deep trap states originated from oxygen vacancy associated with F^+ center. Photoluminescence is mostly a surface phenomenon, and a change in the surface environment would have a significant effect on the photoluminescence process. Due to a large surface area and strong presence of defects in the nanoribbons, defect related PL emission is found to be strong. The emission at 611.7 nm may be assigned to electron transition from the F^+ center to the acceptor level just above the valence band. The presence of hydroxyl (OH) species is detected in the XPS and FTIR spectra, discussed later in this manuscript, which may form an acceptor level just above the valence band and may be responsible for the observed 611.7 nm PL emission. Recently, Yang *et al.* assigned the PL bands at 520 nm (2.38 eV) and 568 nm (2.18 eV) to the oxygen vacancies in TiO_2 nanotubes.⁴⁴ Note that out of the integrated PL intensity, 82% PL in S1 and 90% PL in S4 are related to oxygen vacancies with two orders of magnitude increase in overall intensity of oxygen vacancy (O_v) peaks after vacuum annealing. From our XPS studies, we observed that Ti^{3+} and O_v concentrations are significantly increased in sample S4. This strongly suggests that the concentration of oxygen vacancies is increased considerably in the vacuum annealed sample consistent with the PL analysis. Note that all the PL peaks are red shifted for vacuum annealed sample S4 indicating that the number of defects states increases and overlapping of this large number of defect states broadens the Ti^{3+} center states as well as F^+ center states leading to a narrow bandgap. It was found that the width of the band related to the concentration of Ti^{3+} or oxygen vacancies increased as the concentration of oxygen vacancies increased from 1 per 32 to 1 per 16 oxygen atoms.³⁶ Guillemot *et al.*⁴⁵ reported that the low temperature vacuum annealing could create a controlled number of defects ranging from low concentration ($<3\% \text{Ti}^{3+}/\text{Ti}^{4+}$) to high concentration ($\sim 21\% \text{Ti}^{3+}/\text{Ti}^{4+}$) at 323 and 573 K, respectively. Liu *et al.*⁴⁶ reported that concentration of both Ti^{3+} and oxygen vacancies are increased with H_2 treatment temperature up to 500 °C. This literature is consistent with our observation of the vacuum annealed sample and provides convincing evidence that different concentrations of oxygen vacancies are present in these TiO_2 nanoribbons. Integrated PL intensities for different samples are shown in Table 1. Note that the integrated PL intensity is high in the precursor TiO_2 powders.

XPS studies

XPS is an unique tool to investigate surface defects and chemical environment, because of its high sensitivity to surface. Evidence of oxygen vacancy related surface defect states in samples S1 and S4 is further confirmed from the XPS measurements. To investigate the surface defect states such as Ti^{3+} and F^+ , Ti 2p and O 1s core levels were measured. Fig. 7(a) and (b) show the O 1s spectra of samples S1 and S4, respectively. Both the O 1s spectra exhibit an asymmetric curve and a broad shoulder to the higher binding energy side, indicating that several oxygen species are present in the near surface region.⁴⁷ The O 1s spectra can be deconvoluted by four symmetric

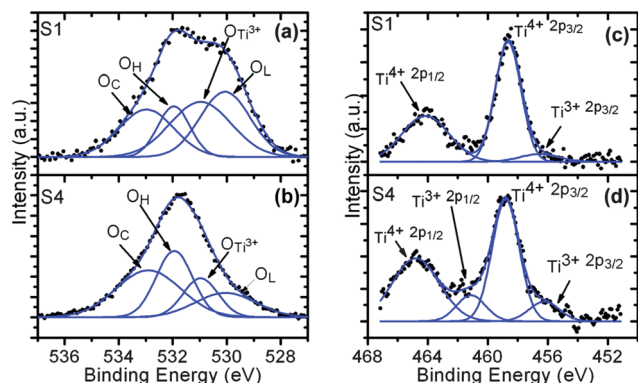


Fig. 7 XPS spectra: (a) and (b) show the O 1s core level spectra of samples S1 and S4, respectively. Symbols are for experimental data and the solid lines are fits with Gaussian peak shapes. (c) and (d) show the Ti 2p core level spectra of samples S1 and S4, respectively.

Gaussian curves, similar to that reported in the literature.⁴⁷ The intense peak at about 530.1 eV is attributed to the oxygen in the TiO₂ crystal lattice (O_L), while the other three oxygen peaks can be assigned to the Ti–O bonds (O_{Ti³⁺}, 531.0 eV), the hydroxyl group (O_H, 532.0 eV), and the C–O bonds (O_C, 532.9 eV), respectively.^{47,48} By comparing the contribution of each type of the oxygen species in the samples S1 and S4, it is observed that the intensity of O_{Ti³⁺} increases along with increase in O_H and O_C peaks for the sample S4 compared to S1. This result reveals that the O_{Ti³⁺} defect concentration dramatically increases after vacuum annealing of S1, which increases the reactivity and binds more hydrogen and carbon as impurities.

Fig. 7(c) and (d) show the Ti 2p core level spectra of samples S1 and S4, respectively. For the sample S1, the deconvolution of Ti 2p core level yields two major characteristic doublets for Ti 2p_{3/2} and 2p_{1/2}, encompassing a set of two 2p_{3/2} peaks at 456.5 eV and 458.6 eV. The 456.5 eV peak is attributed to 3+, while the 458.6 eV peak is assigned to 4+ valence states of Ti, respectively. This result demonstrates that Ti⁴⁺ ions near oxygen vacancies occupy an electron from the oxygen vacancy cavity V_o and transform to Ti³⁺ ions yielding an F[•] center. Similarly for the sample S4, the deconvolution of Ti 2p core level yields two major characteristic doublets (2p_{3/2}, 2p_{1/2}), encompassing a set of two 2p_{3/2} (456.2, 458.8 eV) and two 2p_{1/2} (461.1, 464.8 eV) peaks. The peaks at 458.8 eV and 464.8 eV are attributed to 4+ valence state for Ti 2p_{3/2} and 2p_{1/2}, respectively, while 456.2 eV and 461.1 eV are assigned to 3+ valence state for Ti 2p_{3/2} and 2p_{1/2}, respectively. This additional 3+ valence state of Ti 2p_{1/2} and the increased intensity of Ti³⁺ 2p_{3/2} for the sample S4 strongly indicates that high concentration of oxygen vacancies are created in the reduced atmosphere that results in the increase of Ti³⁺ states. We noticed that after vacuum annealing, the Ti³⁺ concentration is nearly doubled and the intensity of Ti³⁺ band increases along with significant increase in intensity of O_H and O_C peaks due to the dramatic increase in defects in S4. The relative Ti³⁺% and O_v% in Ti 2p and O 1s spectra, respectively are provided in Table 1. Both S1 and S4 show high concentration of oxygen vacancies. These results are fully consistent with the PL analysis and provide rather direct evidence that oxygen

vacancies accompanied by Ti³⁺ are the dominant defects in the as-grown and vacuum annealed TiO₂ nanoribbons.

FTIR studies

FTIR spectroscopy has been employed to investigate the vibration modes of the TiO₂ crystal lattice, which are considerably affected by the presence of oxygen vacancies. Fig. 8(a) shows the FTIR spectra in transmission mode of as-synthesized nanostructures. The absorption peaks around 1600 and 3400 cm^{−1} are due to the adsorption of atmospheric water on the surface of the samples.⁴⁹ The vibration modes at 476, 774, and 980 cm^{−1} are assigned to TiO₂(B) phase^{28,50} and the vibration modes at 574 and 708 cm^{−1} are assigned to anatase TiO₂. The vibration mode at 476 cm^{−1} of TiO₂(B) slightly shifted to higher wave number is due to the phase transition from TiO₂(B) to mixed phase TiO₂(B)–anatase and anatase–rutile, as shown in the inset of Fig. 8(a). Fig. 8(b) shows the FTIR spectra of as-synthesized sample S1 and vacuum annealed sample S4. The characteristic vibration modes of TiO₂(B) phase is observed in vacuum annealed sample indicating the sample retains its phase after vacuum annealing and it is consistent with the Raman analysis. However, an obvious red shift of vibration modes at 476 cm^{−1} to 470 cm^{−1} is observed after vacuum annealing and it is attributed to the higher concentration of oxygen vacancies induced by vacuum

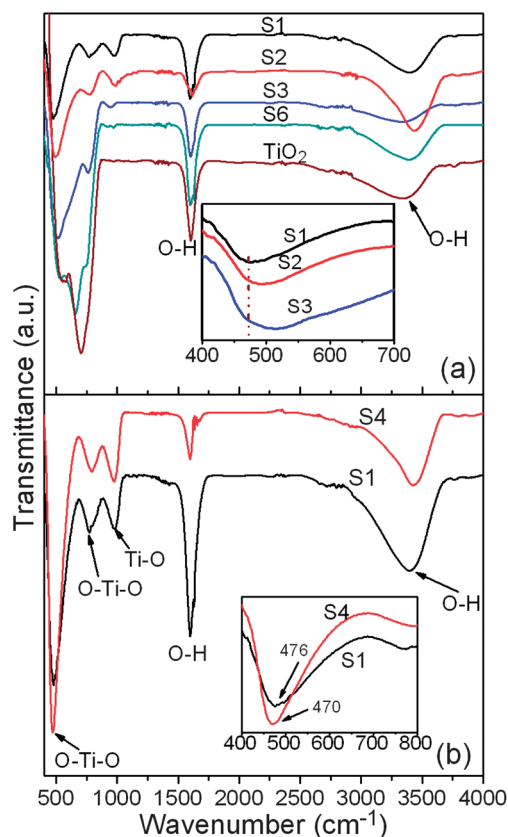


Fig. 8 FTIR spectra: (a) samples S1, S2, S3, S6, and precursor TiO₂. (b) samples S1 and S4. The inset in (a) and (b) show the shifting of the vibration modes.

annealing. A similar shift is reported in Co doped TiO_2 system and it was suggested that the shift was due to the oxygen vacancy.⁵¹ Further, we noticed that the vibration mode at 774 cm^{-1} is blue shifted and 980 cm^{-1} is red shifted in the vacuum annealed sample. Note that the vibration modes at 476 , and 980 cm^{-1} are due to the O–Ti–O bending and Ti–O stretching vibrations, respectively, while 774 cm^{-1} is due to O–Ti–O bending and Ti–O stretching vibrations in $\text{TiO}_2(\text{B})$.³¹ So, the shifting of the vibration bands is expected due to the presence of oxygen vacancies. We also observed the shift of vibration modes at 574 and 708 cm^{-1} towards a lower frequency in the as-synthesized anatase sample S6 compared to the precursor anatase TiO_2 powder, as shown in Fig. 8(a). Such a shift is expected due to oxygen vacancies in our as-synthesized samples, which manifest in interesting room temperature ferromagnetism discussed below.

Magnetic measurements

The magnetic properties of as-synthesized samples were investigated using VSM. The field dependent magnetic (M–H) measurements are shown in Fig. 9. Fig. 9(a) shows clear ferromagnetic hysteresis loops for samples S5, S6, and S7. The samples S5 and S6 show large magnetic moments compared to sample S7. Moreover, S6 shows the higher magnetic moment

than that of S5. Fig. 9(b) shows the M–H loops of the samples S1, S2, and S3. These samples show clear hysteresis loops at low field, but lacks the saturation magnetization, perhaps due to paramagnetic contribution from the conduction electron.⁵² Note that the magnetic moment is relatively higher for S2 and this may be related to the nanobrick-like surface morphology of S2 and/or due to mixed phase of $\text{TiO}_2(\text{B})$ –anatase. It has been reported that the FM is sensitive to the shape and size of the nanostructures. Note that the samples (S5, S6, S7) grown at 180°C after 24 h and 48 h are nanoporous nanoribbons with nanobrick-like structures on the surface. Such complex structures may contain a large concentration of defects, supported by our PL and XPS analyses. The concentration of oxygen vacancies are found to depend on the different surface morphologies and size of the nanostructures, which is the reason for the observed different magnetic moments. Nanosize TiO_2 usually shows weak FM at RT and the FM depends very much on the synthesis procedure, due to the different defects, especially the oxygen vacancies in TiO_2 nanomaterials. One of the most important reasons of relatively strong ferromagnetism in our samples may come from the formation of porous like structures, since we are using ethylene glycol as a cosolvent which has chelating properties. Due to the chelating properties of ethylene glycol, it forms several bonds with metal ions and form cage like structures which helps the formation of porous structure creating more oxygen vacancies. Further, it has been reported that the oxygen vacancies induce lattice distortion in rutile TiO_2 and induces strong FM in undoped TiO_2 films due to charge redistribution.²⁴ The magnitude of the magnetic moment in the rutile phase was predicted to be about four times higher than that in anatase TiO_2 . This is consistent with the observation of highest magnetic moment seen in sample S6 with a mixed rutile-anatase phase as compared to S5 and S7 with $\text{TiO}_2(\text{B})$ phase.

It is well known that the structure of TiO_2 is very sensitive to oxygen and can be easily reduced under an oxygen deficient environment. Therefore, the sample S1 was annealed at 300°C under moderate vacuum in order to induce a higher concentration of oxygen vacancies in the sample. Interestingly, the vacuum annealed sample S4 shows enhanced ferromagnetism with a well-defined hysteresis loop having saturation magnetization (M_s) of 0.191 emu g^{-1} , remanent (M_r) of 0.02 emu g^{-1} and coercive field (H_c) of 99 Gauss, as shown in Fig. 9(c). Such enhancement of FM in oxygen deficient TiO_2 nanoribbons strongly suggests that RTFM and concentration of oxygen vacancies are directly correlated. Indeed the samples exhibiting a high intensity of visible PL (see inset of Fig. 6(a)) only show clear ferromagnetic hysteresis loops with saturation magnetisation plateau. Note that the observed M_s at room temperature in our undoped TiO_2 nanoribbons is more than three times higher than that reported for Fe and N co-doped TiO_2 nanorods⁵³ and other reported literatures.^{28,53,54} Achievement of such a high magnetic moment in defect engineered undoped TiO_2 is remarkable and our studies provide convincing evidence that oxygen vacancies indeed mediate the ferromagnetic interaction. The magnetization parameters for different samples are listed in Table 2.

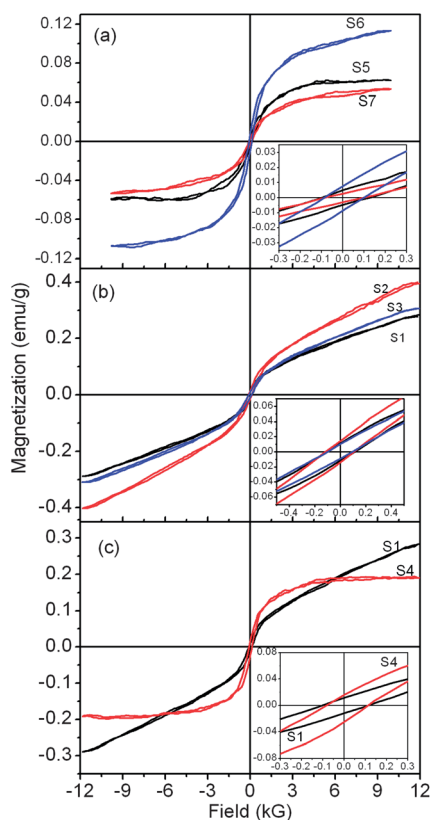


Fig. 9 Magnetic field versus magnetization (M–H) loop at room temperature showing hysteresis in as-synthesized samples: (a) S5, S6 and S7; (b) S1, S2 and S3; (c) S1 and S4. The insets show the magnified M–H loop showing clear ferromagnetic hysteresis behaviour.

It is understood that for use in a wide range of applications without temperature control, the ferromagnet should have a T_c enough above RT (300 K). Fig. 10 shows the temperature dependent magnetization (M - T) of the sample S7 in the temperature range 290 to 860 K. Since the effect of high temperature VSM measurement in atmospheric conditions is equivalent to the post annealing of the as-grown samples in air that can destroy the ferromagnetic coupling, we performed the high temperature VSM measurement in a nitrogen atmosphere. From the differential plot of the M - T curve, we obtained a T_c at ~ 799 K. Interestingly, the gradual increase in magnetization from 290 K to around 334 K is observed in the M - T curve, as shown in the inset of Fig. 10. This indicates that the oxygen vacancies are increased during the early stages of the heating process in a nitrogen atmosphere and these defects contribute to the observed FM. Note that defect mediated bound magnetic polaron (BMP) model has been invoked to explain the RTFM. Due to increased vacancy concentration, more BMPs are available, which include electrons locally trapped by the oxygen vacancy, giving rise to gradual increase in magnetization. The thermal fluctuations of the localized spins may have comparatively less effect in this temperature range. Very recently, Tian *et al.* reported nearly temperature-independent saturation magnetization up to 600 K, which strongly favored the BMP model.⁵⁵ The strength of exchange interaction is stronger in nanostructured magnetic semiconductors where the mean distance between the localized spins is small, which may enhance the thermal stability.

Origin of ferromagnetism

At the present time, there is an incomplete understanding on the origin of ferromagnetism in an undoped TiO_2 semiconductor, whether the Ti vacancy or oxygen vacancy defects are responsible for the observed FM. If the Ti vacancy is the reason for the observed FM in our samples, then ferromagnetic ordering is expected to decrease after vacuum annealing. However, the enhanced magnetic moment with clear saturation magnetization confirms that the FM in our samples is solely due to the oxygen vacancy, since no other impurities are present. Several features, *e.g.*, relative shift, broadening and reduction in intensity of Raman modes at 142 cm^{-1} , systematic shift in infrared band at 476 cm^{-1} towards lower frequency, oxygen vacancy related strong visible PL emission, high oxygen vacancy and Ti^{3+} concentrations observed from XPS spectra and stronger ferromagnetic ordering in vacuum annealed sample provides strong evidence that the observed FM in undoped TiO_2

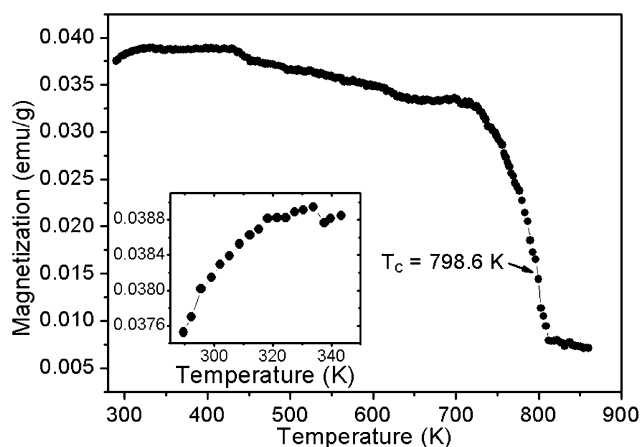


Fig. 10 Temperature dependent magnetization (M - T) curve of sample S7 showing a ferromagnetic to paramagnetic transition at 799 K.

nanoribbons is induced by oxygen vacancies. The presence of an oxygen vacancy on the surface of TiO_2 locally traps the electrons forming F center and one of the electrons tends to occupy the nearby localized Ti 3d orbit and convert Ti^{4+} ions to Ti^{3+} ions, yielding F^+ center. The electrons in F^+ center localize and may form bound magnetic polarons by ordering the Ti^{3+} ($3d^1$) electron spin neighboring the oxygen vacancies, thereby gaining exchange energy. The s-d exchange interaction between the $1s^1$ electron spin in the F^+ center which is localized in the vicinity of $3d^1$ electron spin of Ti^{3+} ions within an orbit around oxygen vacancies favors long range FM. The electrons in doubly occupied oxygen vacancies (F center) form $1s^2$ state, which only mediates weak antiferromagnetic exchange.⁵⁶ Thus the formation of BMP, which includes electrons locally trapped by oxygen vacancies, with the trapped electron in the F^+ center occupying an orbital overlapping with the unpaired electron ($3d^1$) of Ti^{3+} is proposed to explain the origin of FM observed in our samples.

Theoretical studies suggested that oxygen vacancies can cause an obvious change of band structure of the host oxides and makes a significant contribution to the FM.^{56,57} The absorption edges of as-synthesized nanoribbons are red shifted compared to the precursor TiO_2 powder, which may increase the overlapping of oxygen vacancies with the empty conduction band and favor the observed FM. Note that the precursor TiO_2 powder did not show any trace of FM, despite the presence of a large concentration of oxygen vacancies as evidenced by a strong visible PL band (see Table 1). Note that integrated visible PL intensities in S4 and precursor TiO_2 powder are comparable.

Table 2 Magnetization parameters of the as-synthesized and vacuum annealed samples: saturation magnetization (M_s), remanent magnetization (M_r), and Coercive field (H_c) were determined from M - H loops; M_0 , m_{eff} , χ_m , N were evaluated from fitting of the M - H curve with BMP model

Sample name	M_s (emu g ⁻¹)	M_r (emu g ⁻¹)	H_c (Gauss)	M_0 (emu g ⁻¹)	$m_{\text{eff}} \times 10^{-17}$ (emu)	$\chi_m \times 10^{-6}$ (cgs)	$N \times 10^{15}$ (cm ⁻³)
S4	0.191	0.02	99	0.190	8.86	1.32	8.83
S5	0.061	0.005	115	0.070	6.21	0.22	4.63
S6	0.109	0.008	93	0.097	8.28	2.17	4.77
S7	0.054	0.003	90	0.048	6.54	1.02	3.02

Thus, concentration of defects such as oxygen vacancies alone does not decide the magnitude of magnetic moment. Our results suggest that the defect environment and the surface morphology of the nanoribbons, in particular the nanopores and nanobrick like structures, are critical ingredients for the build up of measurable ferromagnetic interaction. This is also consistent with the fact that the TiO₂ nanoribbon with a smooth surface (sample S3) does not show any saturation magnetisation in the M–H loop, though it shows considerable visible PL.

Note that the relatively weak ferromagnetic hysteresis loops for the samples S1, S2, S3 observed at low magnetic field may be due to oxygen vacancies and linear behavior observed at high field without any saturation magnetic moment up to 12 kG may be due to the conduction band electrons.⁵² When the oxygen content of the unit cell is decreased, ferromagnetism is dominant. Interestingly, we notice a clear hysteresis loop with enhanced magnetic properties in terms of M_s , M_r and H_c in the vacuum annealed sample owing to an increase in oxygen vacancy concentrations that may increase the BMP. This seems to support the percolation model of BMP developed by Kaminski and Das Sarma and Coey *et al.*^{56,58} Our systematic study shows that the oxygen vacancy defect constituted BMP is one of the most promising candidates to manifest the RTFM in this system. Within the BMP model, the greater density of the oxygen vacancy helps to produce more BMP which yields a greater overall volume occupied by BMP, leading to an overlap of BMPs and enhancing ferromagnetic behaviour. This evolution is observed in our case, enhancing the ferromagnetic nature in the post-growth vacuum annealed sample indicating that a large density of defects overcomes the percolation threshold and establishes a long-range magnetic ordering.

For a more quantitative understanding about the suitability of the BMP model and its relationship to the oxygen vacancy concentration as revealed from PL spectra, we attempted to fit the observed M versus H data to the BMP model by following Chiorescu *et al.*⁵⁹ According to the BMP model, the measured magnetization can be fitted to the relation

$$M = M_0 L(x) + \chi_m H, \quad (5)$$

where the first term is from BMP contribution and the second term is due to paramagnetic matrix contribution. Here $M_0 = Nm_s$, N is the number of BMP involved (per gram) and m_s is the effective spontaneous moment per BMP. $L(x) = \coth(x) - 1/x$ is the Langevin function with $x = m_{\text{eff}}H/k_B T$, where m_{eff} is the true spontaneous moment per BMP, and at higher temperature it can be approximated to $m_s = m_{\text{eff}}$. We have analyzed the M–H curve by using eqn (5). The parameters M_0 , m_{eff} , and χ_m are variable in the fitting process. The experimental data along with the fitted data are shown in Fig. 11 for the samples S6 and S7. We notice that the fitted data closely follows the experimental data and the fitted parameters are tabulated in Table 2. The total BMP magnetization M_0 values are found to be in the order of 0.048–0.19 emu g^{−1}. The paramagnetic susceptibility χ_m is found to be of the order of 10^{−6} cgs unit and its value marginally changes with different growth conditions. The spontaneous moment per BMP, m_{eff} is found to be in the order of 10^{−17} emu.

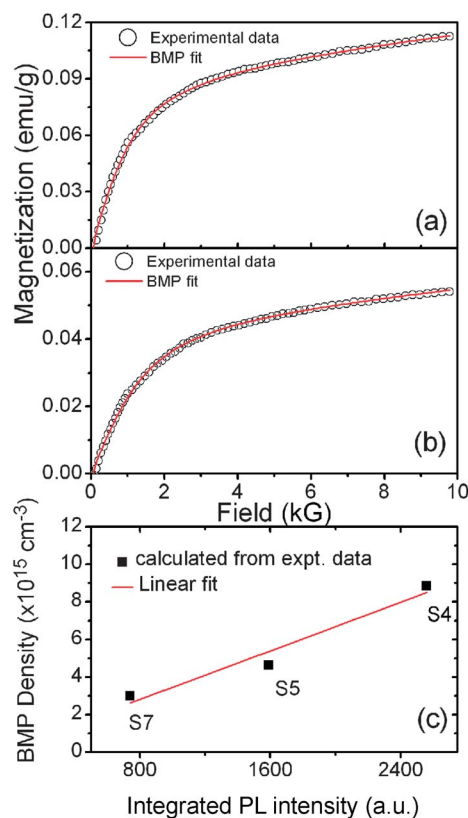


Fig. 11 Initial portion of the M–H curve fitted with BMP model (eqn (5)) for samples (a) S6 and (b) S7. Symbols are for experimental data and the solid line is a fit with the BMP model. Extracted parameters are listed in Table 2. (c) Integrated PL intensity versus calculated BMP density showing a nearly linear behaviour.

By assuming $m_s = m_{\text{eff}}$, we have estimated the concentration of BMP, which was found to be in the order of 10¹⁶ cm^{−3} (see Table 2). Note that BMP concentration is highest in S4, followed by S6, S5 and S7. Interestingly, we found a strikingly linear correlation between the BMP concentration and the integrated PL intensity due to oxygen vacancies, as shown in Fig. 11(c). The symbols are for calculated BMP density from the fitting of experimental data and the solid line is a linear fit to the experimental data. It implies a one to one correlation of the BMP density with oxygen vacancy concentration. Despite the fact that quantitative estimation of defects is rarely possible from the PL intensity comparison due to possible presence of nonradiative channels, one observed correlation is remarkable. This is the first time such a linear relation has been found between the densities of BMP and oxygen vacancies. This provides more conclusive evidence that observed RTFM is directly induced by oxygen vacancies. Recently, in Ag doped ZnO system, He *et al.*⁶⁰ fitted the experimental M–T curve with the BMP model and the concentration of BMP was found to be of the same order ($\sim 10^{15}$) as we found. However, the reported T_c was relatively higher (995 K), though the feature of the M–T curve was identical to our observation. Since the polarons we have described in this system are bound to oxygen vacancies, the term bound magnetic polaron is justified. Interestingly, the BMP remains localized over a wide temperature range,

presumably due to strong localization provided by the defect site and stability of these defects. Note that the as-prepared samples have undergone high temperature calcination that offer high thermal stability of the oxygen vacancies and a large concentration of oxygen vacancies may aid to form even small clusters of vacancies that can provide higher localization of the charges involved in the exchange interaction. However, more studies are required to pinpoint the exact mechanism of high temperature FM. Nevertheless, besides the established applications of TiO₂ nanostructures, these results open up the possibility of defect engineered TiO₂ nanostructures as potential platform for future spintronic and magneto-optic devices.

Conclusions

We successfully prepared undoped TiO₂ nanoporous nanoribbons and investigated the origin of room temperature ferromagnetism in this novel system using several experimental tools. Micro-Raman studies show systematic shift, broadening and decrease in intensity of E_g(1) and B_{1g} Raman modes in as-synthesised and vacuum annealed samples. The enhanced intensity of oxygen vacancy related peak in PL spectra, large concentration of O_V and Ti³⁺ states revealed from XPS, shifting of infrared vibration modes at 476 cm⁻¹ towards the lower frequency after vacuum annealing confirm the presence of large concentration of oxygen vacancies and these are shown to be responsible for the enhanced FM in as-grown and vacuum annealed sample. The observed RTFM is explained on the basis of a BMP model and extracted density of BMP is shown to directly scale with the integrated PL intensity that arises from oxygen vacancies. Thus, our results provide convincing evidence for oxygen vacancy induced strong ferromagnetism at and above room temperature in the undoped TiO₂ nanoporous nanoribbons. These findings not only help to gain better insight into the defect engineering of RTFM in undoped TiO₂, but also constitute an important step for the development of practical nanospintronic devices which can be operated at and above RT. Further, the highly porous TiO₂ nanoribbons developed in this work is an important step towards achieving improved visible light photocatalytic and photovoltaic applications of these materials.

Acknowledgements

This work was partly supported by JSPS Invitation Fellowship, Japan, awarded to PKG.

References

- 1 S. A. Wolf, D. D. Awschalom, R. A. Buhrman, J. M. Daughton, S. Von Molnar, M. L. Roukes, A. Y. Chtchelkanova and D. M. Treger, *Science*, 2001, **294**, 1488.
- 2 H. Ohno, *Science*, 1998, **281**, 951.
- 3 Y. Matsumoto, M. Murakami, T. Shono, T. Hasegawa, T. Fukumura, M. Kawasaki, P. Ahmet, T. Chikyow, S. Koshihara and H. Koinuma, *Science*, 2001, **291**, 854.
- 4 B. Pal and P. K. Giri, *J. Appl. Phys.*, 2010, **108**, 084322.
- 5 X. Liu, J. Iqbal, Z. Wu, B. He and R. Yu, *J. Phys. Chem. C*, 2010, **114**, 4790.
- 6 G. Z. Xing, J. B. Yi, D. D. Wang, L. Liao, T. Yu, Z. X. Shen, C. H. A. Huan, T. C. Sum, J. Ding and T. Wu, *Phys. Rev. B: Condens. Matter Mater. Phys.*, 2009, **79**, 174406.
- 7 B. Santara, B. Pal and P. K. Giri, *J. Appl. Phys.*, 2011, **110**, 114322.
- 8 J.-Y. Kim, J.-H. Park, B.-G. Park, H.-J. Noh, S.-J. Oh, J. S. Yang, D.-H. Kim, S. D. Bu, T.-W. Noh, H.-J. Lin, H.-H. Hsieh and C. T. Chen, *Phys. Rev. Lett.*, 2003, **90**, 017401.
- 9 J. Xu, S. Shi, L. Li, X. Zhang, Y. Wang, X. Chen, J. Wang, L. Lv, F. Zhang and W. Zhong, *J. Appl. Phys.*, 2010, **107**, 053910.
- 10 K. G. Roberts, M. Varela, S. Rashkeev, S. T. Pantelides, S. J. Pennycook and K. M. Krishnan, *Phys. Rev. B: Condens. Matter Mater. Phys.*, 2008, **78**, 014409.
- 11 P. Mohanty, N. C. Mishra, R. J. Choudhary, A. Banerjee, T. Shripathi, N. P. Lalla, S. Annapoorni and C. Rath, *J. Phys. D: Appl. Phys.*, 2012, **45**, 325301.
- 12 T. Tietze, M. Gacic, G. Schütz, G. Jakob, S. Brück and E. Goering, *New J. Phys.*, 2008, **10**, 055009.
- 13 M. Gacic, G. Jakob, C. Herbolt, H. Adrian, T. Tietze, S. Brück and E. Goering, *Phys. Rev. B: Condens. Matter Mater. Phys.*, 2007, **75**, 205206.
- 14 Q. Xu, H. Schmidt, L. Hartmann, H. Hochmuth, M. Lorenz, A. Setzer, P. Esquinazi, C. Meinecke and M. Grundmann, *Appl. Phys. Lett.*, 2007, **91**, 092503.
- 15 S. K. Pandey and R. J. Choudhary, *J. Phys.: Condens. Matter*, 2011, **23**, 276005.
- 16 N. T. Q. Hoa and D. N. Huyen, *J. Mater. Sci.: Mater. Electron.*, 2013, **24**, 793.
- 17 N. H. Hong, J. Sakai, N. Poirot and V. Brize, *Phys. Rev. B: Condens. Matter Mater. Phys.*, 2006, **73**, 132404.
- 18 M. Venkatesan, C. B. Fitzgerald and J. M. D. Coey, *Nature*, 2004, **430**, 630.
- 19 N. H. Hong, N. Poirot and J. Sakai, *Phys. Rev. B: Condens. Matter Mater. Phys.*, 2008, **77**, 033205.
- 20 X. Xu, C. Xu, J. Dai, J. Hu, F. Li and S. Zhang, *J. Phys. Chem. C*, 2012, **116**, 8813.
- 21 G. Yang, D. Gao, J. Zhang, J. Zhang, Z. Shi and D. Xue, *J. Phys. Chem. C*, 2011, **115**, 1681.
- 22 A. Sundaresan and C. N. R. Rao, *Nano Today*, 2009, **4**, 96.
- 23 H. Peng, J. Li, S.-S. Li and J.-B. Xia, *Phys. Rev. B: Condens. Matter Mater. Phys.*, 2009, **79**, 092411.
- 24 D. Kim, J. Hong, Y. R. Park and K. J. Kim, *J. Phys.: Condens. Matter*, 2009, **21**, 195405.
- 25 A. K. Rumaiz, B. Ali, A. Ceylon, M. Boggs, T. Beebe and S. I. Shah, *Solid State Commun.*, 2007, **144**, 334.
- 26 H. Li, Y. Zeng, T. Huang and M. Liu, *J. Nanopart. Res.*, 2012, **14**, 1030.
- 27 L. Hong-mei, L. Min, Z. Yang-su and H. Tong-cheng, *J. Cent. South Univ. Technol.*, 2010, **17**, 239.
- 28 S. K. S. Patel and N. S. Gajbhiye, *Solid State Commun.*, 2011, **151**, 1500.
- 29 M. Zúkalová, M. Kalbáč, L. Kavan, I. Exnar and M. Graetzel, *Chem. Mater.*, 2005, **17**, 1248.
- 30 D. Yang, H. Liu, Z. Zheng, Y. Yuan, J. Zhao, E. R. Waclawik, X. Ke and H. Zhu, *J. Am. Chem. Soc.*, 2009, **131**, 17885.

- 31 M. B. Yahia, F. Lemoigno, T. Beuvier, J.-S. Filhol, M. Richard-Plouet, L. Brohan and M.-L. Doublet, *J. Chem. Phys.*, 2009, **130**, 204501.
- 32 J. C. Parker and R. W. Seigel, *Appl. Phys. Lett.*, 1990, **57**, 943.
- 33 W. F. Zhang, Y. L. He, M. S. Zhang, Z. Yin and Q. Chen, *J. Phys. D: Appl. Phys.*, 2000, **33**, 912.
- 34 X. Jiang, Y. Wang, T. Herricks and Y. Xia, *J. Mater. Chem.*, 2004, **14**, 695.
- 35 I. Justicia, P. Ordejon, G. Canto, J. L. Mozos, J. Fraxedes, G. A. Battiston, R. Gerbasi and A. Figueras, *Adv. Mater.*, 2002, **14**, 1399.
- 36 F. Zuo, L. Wang, T. Wu, Z. Zhang, D. Borchardt and P. Feng, *J. Am. Chem. Soc.*, 2010, **132**, 11856.
- 37 J. Wang, Z. Wang, B. Huang, Y. Ma, Y. Liu, X. Qin, X. Zhang and Y. Dai, *ACS Appl. Mater. Interfaces*, 2012, **4**, 4024.
- 38 S. Hoang, S. P. Berglund, N. T. Hahn, A. J. Bard and C. B. Mullins, *J. Am. Chem. Soc.*, 2012, **134**, 3659.
- 39 J. Shi, J. Chen, Z. Feng, T. Chen, Y. Lian, X. Wang and C. Li, *J. Phys. Chem. C*, 2007, **111**, 693.
- 40 N. Serpone, *J. Phys. Chem. B*, 2006, **110**, 24287.
- 41 N. Serpone, D. Lawless and R. Khairutdinov, *J. Phys. Chem.*, 1995, **99**, 16646.
- 42 L. V. Saraf, S. I. Patil, S. B. Ogale, S. R. Sainkar and S. T. Kshisager, *Int. J. Mod. Phys. B*, 1998, **12**, 2635.
- 43 Y. Lei, L. D. Zhang, G. W. Meng, G. H. Li, X. Y. Zhang, C. H. Liang, W. Chen and S. X. Wang, *Appl. Phys. Lett.*, 2001, **78**, 1125.
- 44 M. Yang, W. Liu, J.-L. Sun and J.-L. Zhu, *Appl. Phys. Lett.*, 2012, **100**, 043106.
- 45 F. Guillemot, M. C. Porté, C. Labrugère and C. Baquey, *J. Colloid Interface Sci.*, 2002, **255**, 75.
- 46 H. Liu, H. T. Ma, X. Z. Li, W. Z. Li, M. Wu and X. H. Bao, *Chemosphere*, 2003, **50**, 39.
- 47 J. Zhuang, S. Weng, W. Dai, P. Liu and Q. Liu, *J. Phys. Chem. C*, 2012, **116**, 25354.
- 48 J. C. Yu, J. Yu, H. Y. Tang and L. Zhang, *J. Mater. Chem.*, 2002, **12**, 81.
- 49 T. M. H. Costa, M. R. Gallas, E. V. Benvenutti and A. H. Jornada, *J. Phys. Chem. B*, 1999, **103**, 4278.
- 50 S. Chatterjee, K. Bhattacharyya, P. Ayyub and A. K. Tyagi, *J. Phys. Chem. C*, 2010, **114**, 9424.
- 51 K. Das, S. N. Sharma, M. Kumar and S. K. De, *J. Phys. Chem. C*, 2009, **113**, 14783.
- 52 A. Sundaresan, R. Bhargvi, N. Rangarajan, U. Siddesh and C. N. R. Rao, *Phys. Rev. B: Condens. Matter Mater. Phys.*, 2006, **74**, 161306(R).
- 53 H. Wang, J. Wei, R. Xiang and J. Shi, *J. Magn. Magn. Mater.*, 2012, **324**, 2057.
- 54 S. K. S. Patel and N. S. Gajbhije, *J. Magn. Magn. Mater.*, 2013, **330**, 21.
- 55 Y. Tian, Y. Li, M. He, I. A. Putra, H. Peng, B. Yao, S. A. Cheong and T. Wu, *Appl. Phys. Lett.*, 2011, **98**, 162503.
- 56 J. M. D. Coey, M. Venkatesan and C. B. Fitzgerald, *Nat. Mater.*, 2005, **4**, 173.
- 57 J. E. Jaffe, T. C. Droubay and A. A. Chambers, *J. Appl. Phys.*, 2005, **97**, 73908.
- 58 A. Kaminski and S. Das Sarma, *Phys. Rev. Lett.*, 2002, **88**, 247202.
- 59 C. Chiorescu, J. L. Cohin and J. J. Neumeier, *Phys. Rev. B: Condens. Matter Mater. Phys.*, 2007, **76**, 020404(R).
- 60 M. He, Y. F. Tian, D. Springer, I. A. Putra, G. Z. Xing, E. E. M. Chia, S. A. Cheng and T. Wu, *Appl. Phys. Lett.*, 2011, **99**, 222511.